

Disorder-induced symmetry breaking in moiré bands of marginally twisted bilayer MoS₂

Pablo Reséndiz-Vázquez^{*1}, Christophe de Beule^{†2,3}, Thi-Hai-Yen Vu¹, Kaijian Xing¹, Daniel McEwen¹, Daniel Bennett^{4,5}, Liangtao Peng⁶, Héctor González-Herrero^{7,8}, Shaffique Adam⁶, Mark T. Edmonds¹, and Michael S. Fuhrer^{‡1}

¹School of Physics and Astronomy, Monash University, Clayton, Victoria 3800, Australia

²Department of Physics and Astronomy, University of Pennsylvania, Philadelphia, Pennsylvania 19104, USA

³Department of Physics, University of Antwerp, Groenenborgerlaan 171, 2020 Antwerp, Belgium

⁴John A. Paulson School of Engineering and Applied Sciences, Harvard University, Cambridge, Massachusetts 02138, USA

⁵School of Electrical and Electronic Engineering, Nanyang Technological University Singapore, 50 Nanyang Avenue, 639798, Singapore

⁶Department of Physics, Washington University, St. Louis, Missouri 63130, USA

⁷Departamento de Física de la Materia Condensada, Universidad Autónoma de Madrid, E-28049 Madrid, Spain

⁸Condensed Matter Physics Center (IFIMAC), Universidad Autónoma de Madrid, E-28049, Madrid, Spain

Abstract

Twisted transition-metal dichalcogenides host highly tunable moiré potentials, flat bands, and correlated electronic phases, yet the role of disorder in shaping these emergent properties remains largely unresolved. Using scanning tunneling spectroscopy, we investigate the impact of electrostatic disorder on the electronic structure of marginally twisted ($\theta \approx 0.95^\circ$) bilayer MoS₂. Differences of 15 meV in the onset energies of the valence and conduction bands between MX and XM stacked regions are observed, and are unexpected due to symmetry considerations. We also observe spatially correlated disorder in the onset energy that is consistent with a background random charge density of a few 10^{11} cm^{-2} . Continuum model calculations for twisted MoS₂ show dramatic changes in the low-energy moiré bands in response to an electric displacement field, in quantitative agreement with experiment. Moreover, the calculated local density of states with disorder smearing compares well to experiment only when structural relaxation is accounted for. These results highlight the critical role of electrostatic disorder in the electronic structure of moiré materials at the nanoscale.

In twisted superstructures (moiré superlattices), such as twisted transition metal dichalcogenides (tTMDs), electron interference gives rise to nearly non-dispersing “flat” bands. These flat bands are known to host strongly correlated electronic phenomena, including generalized Kane–Mele phases [1], fractional quantum anomalous Hall states [2], generalized Wigner crystals [3], Haldane- type [4] and Mott-type insulating phases [5], superconducting states [6] and topologically non- trivial phase transitions [7].

Unlike the paradigmatic case of twisted bilayer graphene, where a single *magic* angle is required for flat bands and the observation of correlated electron states [8, 9], in small-angle tTMDs, theoretical studies predict that the bandwidth of the low-energy moiré bands decreases continuously with twist angles near both parallel (0°) and antiparallel (60°) stacking [10, 11], making them an accessible platform to investigate a rich variety of emergent quantum phases [12, 13].

Although crystallographic growing techniques have considerably advanced in producing high-quality crystals [14], intrinsic disorder persists as an unavoidable feature in two- dimensional (2D) materials [15, 16]. This disorder has been shown to have a strong influence on the electronic properties of these materials, such

^{*}Corresponding author: pab.rv94@gmail.com

[†]Corresponding author: christophe.debeule@uantwerpen.be

[‡]Corresponding author: michael.fuhrer@monash.edu

as modifying the interlayer coupling through local charge redistribution [17], altering lattice relaxation via inhomogeneous local strain fields [18], limiting the mobility of charge carriers [19] or causing Fermi energy fluctuations in Dirac semimetals [20] due to the formation of charge puddles, and even driving quantum phase transitions [21–23].

In TMDs, the formation mechanisms and microscopic nature of disorder, as well as its role in the electronic structure, remains under debate [15, 24]. This naturally raises the question of whether disorder could also play an important role in tTMD moiré systems.

While angle-resolved photoemission spectroscopy (ARPES) [25, 26] and electrical transport measurements [27, 28] have been useful in measuring the band structure of these materials, unambiguously associating disorder with local electronic structure at the nanoscale requires a local probe such as scanning tunneling microscopy (STM) and spectroscopy (STS) [29–31]. These techniques offer a unique way to measure the local density of states (LDOS) that populate such bands as well as its spatial modulation across distinct moiré regions [12].

STM/STS studies have revealed key signatures in the LDOS of small-angle tTMDs. Notable recent examples include the observation of flat bands at the Γ_v point of the first moiré Brillouin zone (mBZ) of antiparallel twisted bilayer WSe₂ over a range of marginal twist angles [29]; the measurement of an LDOS shift close to the valence band maxima between highly symmetric regions in parallel twisted bilayer MoS₂ [30], attributed to the inverse intrinsic electric polarization of these stackings; and the identification of a “special angle” in twisted bilayer MoS₂ at 1.7°, where the bandwidth of the “flat” band at Γ_v reaches a local minimum value of 195 meV [31]. However the role of native disorder in the moiré bands has received little attention.

In this work, we investigate the impact of electrostatic disorder on the moiré band structure of marginally twisted ($\theta \sim 0.9^\circ$) bilayer MoS₂ (tb-MoS₂) using STM/STS. Topographic measurements reveal a reconstructed triangular moiré superlattice with pronounced spatial disorder. Local spectroscopic measurements across distinct stacking regions show an unexpected splitting of the onset energy of the valence and conduction band edges between mirror symmetric moiré sites. We attribute these observations to an interlayer electrostatic potential induced by randomly distributed charged defects, likely sulfur vacancies. By developing an electrostatic disorder model, we infer a background charge density consistent with sulfur vacancy densities reported for exfoliated monolayer MoS₂ [24, 32–34]. We then perform continuum-model calculations of the moiré band structure under symmetry-breaking out-of-plane electric fields consistent with the inferred disorder potential. These calculations reveal a pronounced splitting of the low-energy moiré bands near the valence and conduction band edge, in excellent agreement with our experimental results.

Results

Figure 1 provides an overview of the experiment. Figure 1a schematically illustrates the experimental device setup. Samples were fabricated using the tear-and-stack technique (see Methods section and Supporting information (SI) Figure S1 for more details). Using the STM probe, we observe a large moiré superlattice that emerges when two marginally twisted MoS₂ monolayers undergo lattice relaxation. This moiré structure consists of a hexagonal honeycomb lattice formed by two oppositely arranged triangular domains made of MX (orange) and XM (blue) stacking registries. Here, M (X) represents the Mo (S) atoms, with the letter order indicating the vertical stacking sequence. Thin domain walls (DW) separate the MX/XM regions, while MM registries, for which the Mo atoms of different layers are directly on top of each other, are confined to the vertices of the lattice [35–37], as illustrated in the inset.

Figure 1b shows an STM topograph of the tb-MoS₂ moiré superlattice. The MM regions appear as bright dots, and the domain walls as bright lines. The observed average periodicity is $\lambda_M \simeq 18.7 \pm 0.5$ nm, using $a = 0.31$ nm for the MoS₂ lattice constant [38], yielding a twist angle of $\theta \sim 0.95^\circ \pm 0.03^\circ$.

The scan also reveals topographic disorder that appears correlated on length scales exceeding the moiré period, as well as heterostrain (distortion of the moiré lattice) inherent to the morphology of the sample region. To highlight the superlattice we overlay a dotted white hexagon as a visual guide.

The band structure of tb-MoS₂ was calculated using a continuum model (see Methods and SI for details), with the conduction and valence bands shown in Figures 1c and d, respectively, for $\theta \sim 0.95^\circ$. The effects of atomic relaxation [35, 37, 39, 40] were included in the continuum model (see Methods and SI for details). The vertical energy scales are measured relative to the energies E_c (E_v) of the lowest (highest) energy

moiré miniband derived from the MoS₂ conduction (valence) band, while the color scale represents the layer polarization between the top and bottom MoS₂ layers. Narrow, few-meV-wide bands are observed near the band edges of both conduction and valance bands.

In the conduction band, the first moiré band manifold consists of two nearly degenerate subbands, with weights on the top and bottom layers, respectively. These bands predominantly originate from Mo- d_{z^2} orbitals with only minor contributions from S- p_x and S- p_y orbitals [41]. The interlayer coupling between the top and bottom layers is strong for the MM stacking, but relaxation shrinks these regions to points, hence weak interlayer tunneling results in near-degeneracy of the two subbands (see SI Figure S10b).

In contrast, the valence bands are strongly layer-hybridized. In this case the Wannier orbitals, which originate mostly from the Mo- d_z^2 and S- p_z orbitals [10, 30, 31, 41], are a superposition of states from both layers, coupled through strong interlayer tunelling at MX and XM regions, and the two topmost (spin degenerate) valence bands have a graphene-like character with bonding and anti-bonding subbands crossing at Dirac points at κ/κ' in the mBZ. (see SI Figure S10a).

In order to visualize the spatial variation in LDOS corresponding to the moiré bandstructure, in Figures 1e and f we plot "onset maps", these are spatial distributions of the energies at which the LDOS first rises above an arbitrarily-set value for the conduction and valence band edges, respectively. Here, the LDOS is computed from the moiré continuum model for the top (bottom) of the valence (conduction) band where we sum over both layers of tb-MoS₂ (see Methods section for further details). These onset maps feature the same hexagonal moiré lattice reconstruction observed in the topographic measurements. We can see that in the case of pristine tb-MoS₂, the LDOS shows that the MX and XM states have the same onset energies, which is enforced by a mirror symmetry.

We now measure the electronic structure at the four high-symmetry stacking regions (MM, MX, XM and DW) of the moiré lattice with scanning tunneling spectroscopy (STS), in which the dI/dV spectrum (the differential conductance dI/dV as a function of sample bias V) is proportional to the LDOS at energy $E_F + eV$, where E_F is the Fermi energy. Fig. 2 shows our results.

Figure 2a shows point spectra taken at the high-symmetry stacking regions of the moiré lattice. We observe three main LDOS features: (1) the onset of the valence band LDOS at roughly -1.6 V (labeled Γ_v), (2) the onset of the conduction band LDOS at roughly $+0.3$ V (labeled K_c), and (3) an additional onset of LDOS at approximately -2.2 V (labeled K_v). Through comparison to previous experimental and theoretical work [31, 42–44], we identify these LDOS features as corresponding to the valence band (Γ_v) and conduction band (K_c) edges which arise from states located near the Γ and K/K' points of untwisted bilayer MoS₂, and the onset of LDOS associated with states located near K/K' in the valence band (K_v). No dI/dV signal above the noise floor was observed in the bulk band gap and therefore in order to display the changes in the valence and conduction band edges, the measurements in the gap region were removed.

The valence band edge at Γ_v exhibits several notable features which are analyzed further below. The STS spectra acquired at MM and DW stacking regions show a pronounced shift towards lower bias compared to those measured in the MX and XM domains. On the other hand, the onset energy at MM is shifted towards lower bias relative to the DW onset, similar to the STS characteristics reported in Refs. [30, 31].

The STS spectra at MX and XM stackings appear to show a shift in onset of LDOS at Γ_v , visibly more negative at MX than at XM. As discussed above, since the minibands are predicted to be completely unpolarized, such a shift is unexpected based on the symmetry of the pristine moiré system and it has not been reported in previous works. It is less clear from these point spectra whether a similar onset shift is observed at the conduction band edge at K_c .

In order to further explore and quantify the apparent spatial modulation of the LDOS onsets within several moiré unit cells, we performed STS maps over a region containing around 10 MX/XM domains (see Methods section for further measurement details). From these grid measurements, we extracted onset maps of the onset bias of the LDOS features Γ_v and K_c . Similar to the theoretically obtained, these values are determined by finding the intersection between a noise floor and a linear fit to $\log(dI/dV)$ at the corresponding band edges, following the approach of Refs. [45–47] (see Methods section and SI Figure S2 for further details). The results are shown in Figures 2b and c, respectively. In both onset maps, alternating dark and bright triangles with opposite orientation (highlighted by red dashed lines) can be distinguished. The spatial period matches the one of the moiré lattice obtained from the topography image in Figure 1b. Thus, the triangular shapes are identified as MX/XM domains. Substantial randomly localized onset bias variations at a scale similar to the color contrast between MX/XM regions is also seen in both maps, which

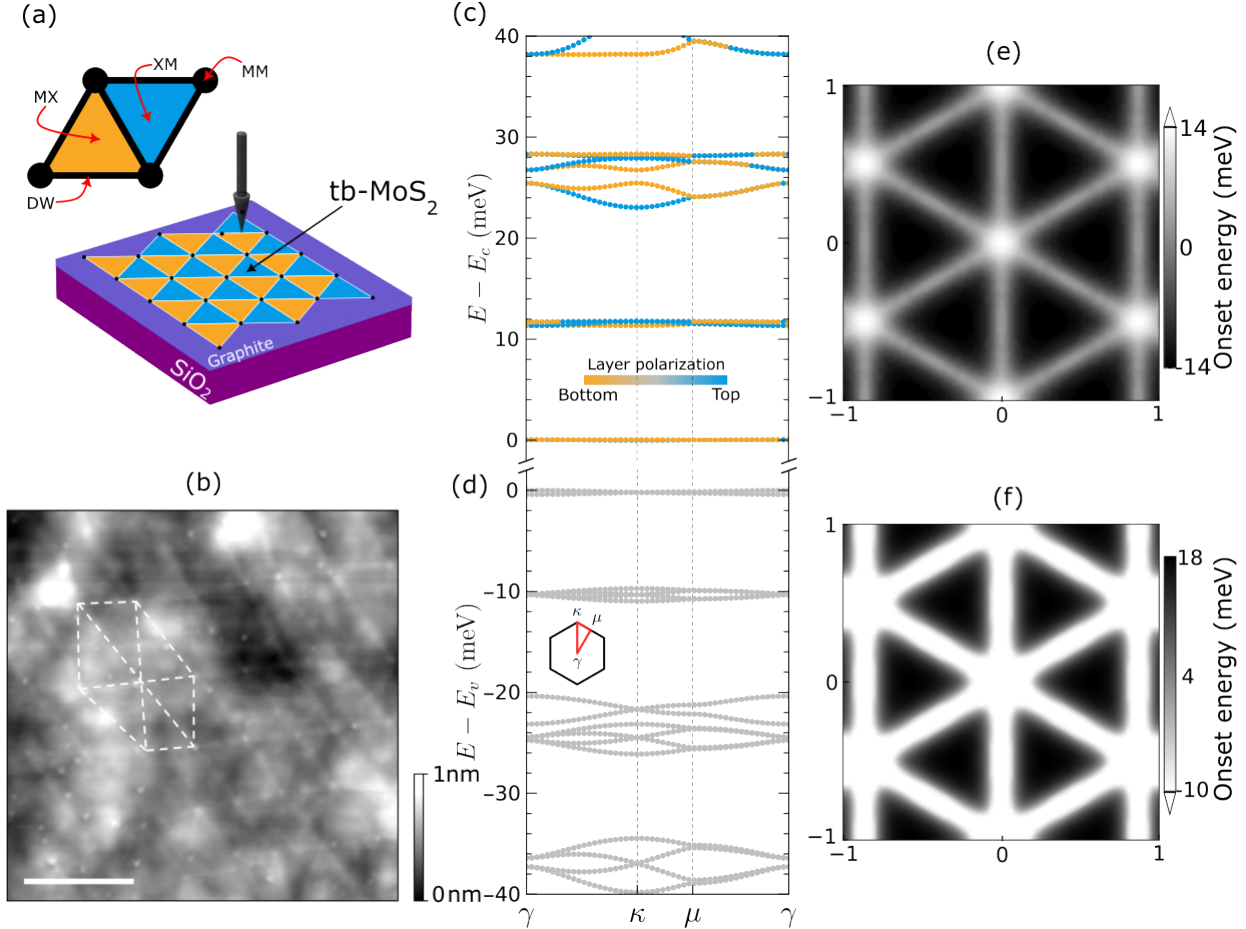


Figure 1: (a) Schematic of the tb-MoS₂ device on a graphite/SiO₂ substrate. The inset shows the structure in a moiré unit cell, with MM sites, MX/XM stacking domains, and DWs. (b) Large area STM topograph of the tb-MoS₂ device showing a moiré lattice with a lattice constant of ~ 18 nm corresponding to a twist angle of $\sim 0.95^\circ$. A dotted white hexagon outlines the domain walls (DW) of a few moiré unit cells. Scale bar: 40 nm. Measurement parameters: $V_{\text{bias}} = -1.9$ V, $I_{\text{set}} = 100$ pA. (c,d) Low-energy bands computed with the continuum model for (c) the conduction and (d) the valence band, along the path $\gamma \rightarrow \kappa \rightarrow \mu$, in the mBZ shown in the inset. The projection of the layer polarization onto the bands is shown, as indicated by the color scale. (e,f) Calculated spatial maps of onset energies for conduction (e) and valence (f) bands showing a honeycomb hexagonal lattice similar to one observed in (a). Given that for some locations the energy intersection with the arbitrarily-set LDOS value does not exist within the energy range, the color bars are unbounded in one direction (indicated by the arrow).

we identify as disorder.

To characterize the average onset shift between several moiré domains, spatially averaged STS curves of the same moiré regions (XM or MX) are obtained. The resulting spectra, shown in Figures 2d and e, reveal a splitting of 15 ± 4 mV between MX and XM sites for the valence band and of 15 ± 6 mV for the conduction band (see Methods for further details).

In order to qualitatively analyze the role of disorder in our measurements, we developed an electrostatic model that allowed us to infer the density of trapped charges and the electric field associated with it. Experimental studies have reported the presence of point defects in exfoliated [24] and in chemical vapor deposited (CVD) MoS₂ monolayers [48]. Among other types of defects, sulfur vacancies (V_S) have been predicted by first-principles calculations [49] and confirmed by STM and TEM experiments [24, 34] to be the

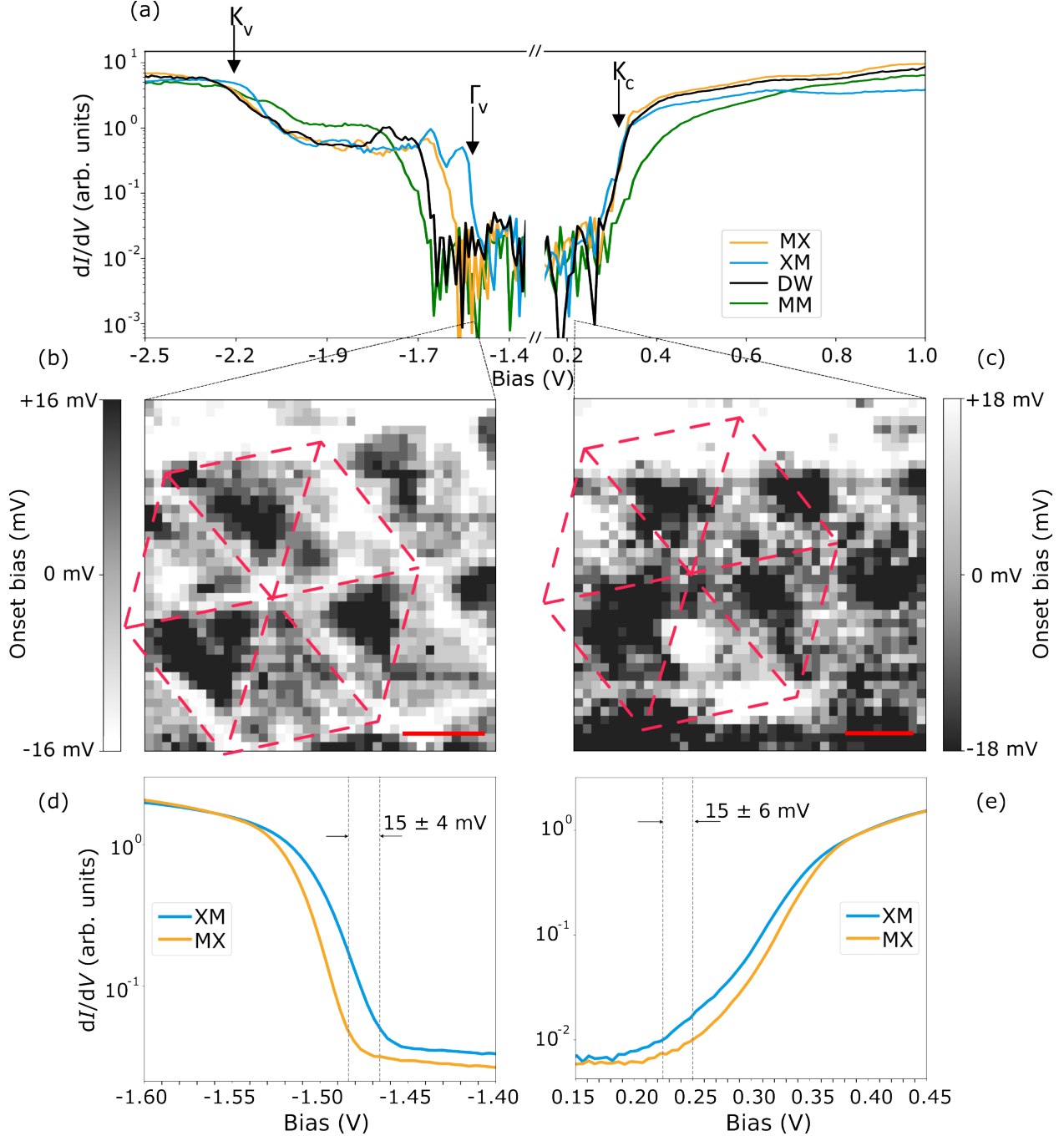


Figure 2: (a) STS point measurements at the AA, MX, XM and DW regions of the moiré lattice. Measurement parameters are $V_{\text{bias}} = -2.5$ V, $I_{\text{set}} = 250$ pA. Each curve is the average of 10 sweeps taken using lock-in amplifier with modulation amplitude of 10 mV and frequency of 793 Hz. (b,c) Onset maps over a $\sim 50 \times 50$ nm 2 moiré region for the valence band (b) and conduction band (c) edges. Red dashed lines highlight some moiré domain walls. Scale bar is 10 nm. (d,e) Spatially averaged LDOS for the MX/XM regions shown in (b) and (c). Vertical dotted lines show the calculated onset energies for each curve, the absolute difference between them and its uncertainty are indicated in each plot. The vertical axis of all the STS curves are in logarithmic scale.

most abundant lattice defects [24, 50]. These V_S centers are stable in neutral or negatively charged states and therefore act as electron acceptors [49]. We assume that our tb-MoS₂ has an areal concentration n_V of negatively-charged V_S randomly distributed in the four S layers, as depicted in Figure 3a.

Figure 3a presents a schematic illustration of the electrostatic disorder model. To obtain the electrostatic potential due to the charges with concentration n_V , we treat the graphite substrate as an ideal metal. This is a reasonable approximation given that thin graphite has a Thomas–Fermi screening length of 5–7 Å [51], which is shorter than the thickness of the twisted-MoS₂ bilayer (~ 12 Å [52]). We then use the textbook method of images [53], applied to a system of alternating thin dielectric layers between a metallic layer underneath and vacuum on top to calculate the average electrostatic potential, $V(x, y)$, generated by randomly distributed charges located within the four sulfur atomic layers of the tb-MoS₂ stack, which are schematically represented by red dots in Figure 3a. At distances $r \gg 2d$ (the thickness of tb-MoS₂) the radial dependence of the potential is $V(r) \sim 1/r^3$, as expected for the dipole of the vacancy charge and its image in the graphite. See Methods section for more details.

To quantitatively compare the model with the experimental data, we assume that the band onsets in Figures 2b and c have a component proportional to the electrostatic disorder potential, $V(x, y)$, in addition to the dependence on the location within the moiré unit cell. We then compute the radially averaged autocorrelation functions, $\phi(r)$ which should reflect the radial dependence of the disorder potential $V(r)$. We fit $\phi(r)$ to $V(r)$ to determine the single fit parameter n_V .

The solid curves in Figures 3b and c are the radial profiles of the onset map's autocorrelation functions associated with the valence and conduction bands, respectively. A positive autocorrelation is observed at small distances, consistent with long-ranged disorder. However a significant spatial modulation in both datasets is evident, which repeats approximately every moiré lattice constant and is due to the large variation of the onset energy within the moiré unit cell, which is not completely removed by radial averaging. To overcome this, we fitted the experimental onset energies in the regime $r > 10$ nm to power laws (dashed lines), obtaining exponents $\alpha = -3.22$ for Γ_v and $\alpha = -3.36$ for K_c , respectively. The exponents are in excellent agreement with the expectation $\alpha = -3$ i.e. $V(r) \sim 1/r^3$ at large r . Figures 3d and e show the experimental $\phi(r)$ at small r along with the model, and the power-law fit to the experimental $\phi(r)$ (dashed lines) for the the Γ_v and K_c onsets respectively. The experimental $\phi(r)$ is systematically lower at small r than predicted from the long-range tail. This may be due to the fact that the onset of LDOS as measured by STS probes a property of the moiré superlattice, and may not measure disorder on length scales smaller than $\lambda_M \sim 20$ nm.

The prefactor of the power-law fit allows us to determine n_V . We obtain two estimates, $n_V = 1 \times 10^{12} \text{ cm}^{-2}$ and $n_V = 3 \times 10^{11} \text{ cm}^{-2}$ (red solid curves) for the Γ_v and K_c onsets respectively. Remarkably, the fitted densities for n_V obtained through our model lie within the reported V_S -associated defect-density range for mechanically exfoliated MoS₂ monolayers of $1 \times 10^{11} \text{ cm}^{-2} - 1 \times 10^{12} \text{ cm}^{-2}$ [24, 32–34] (and below the typical reported defect-densities for CVD-grown crystals of $1 \times 10^{12} \text{ cm}^{-2} - 1 \times 10^{13} \text{ cm}^{-2}$ [54–56]).

Finally, we model the effect of the electric field due to the areal density of charged defects n_V on the moiré bands. We use the continuum model for tb-MoS₂ with $\theta = 0.95^\circ$ under the presence of an interlayer bias potential $V_z = 20$ meV, which corresponds to the electric potential associated with the higher estimated defect density $n_V = 1 \times 10^{12} \text{ cm}^{-2}$. Details of the calculation are given in the Methods section.

Figure 4 shows the results of our calculations. Figures 4a and b show the low-energy moiré bands for finite interlayer bias for the conduction (Figure 4a) and valence (Figure 4b) bands with their layer polarization indicated by the color scale. It can be seen that both valence and conduction bands become layer-polarized. Figures 4c and d show the average LDOS at the MX and XM stacking centers in the moiré cell, respectively, assuming a Lorentzian broadening $\gamma = 10$ meV to account for charged disorder and thermal effects. An onset shift of few tens of meV is observed between the spectra, similar to the experiment (Figures 2d and e). Figures 4e and f we show the calculated onset maps, defined as the energy where the LDOS reaches the value denoted by the dashed lines in Figures 4c and d. A visible color contrast between the triangular MX and XM regions within the moiré unit cell is seen, on the same energy scale as the experimental onset maps (Figures 2b and c).

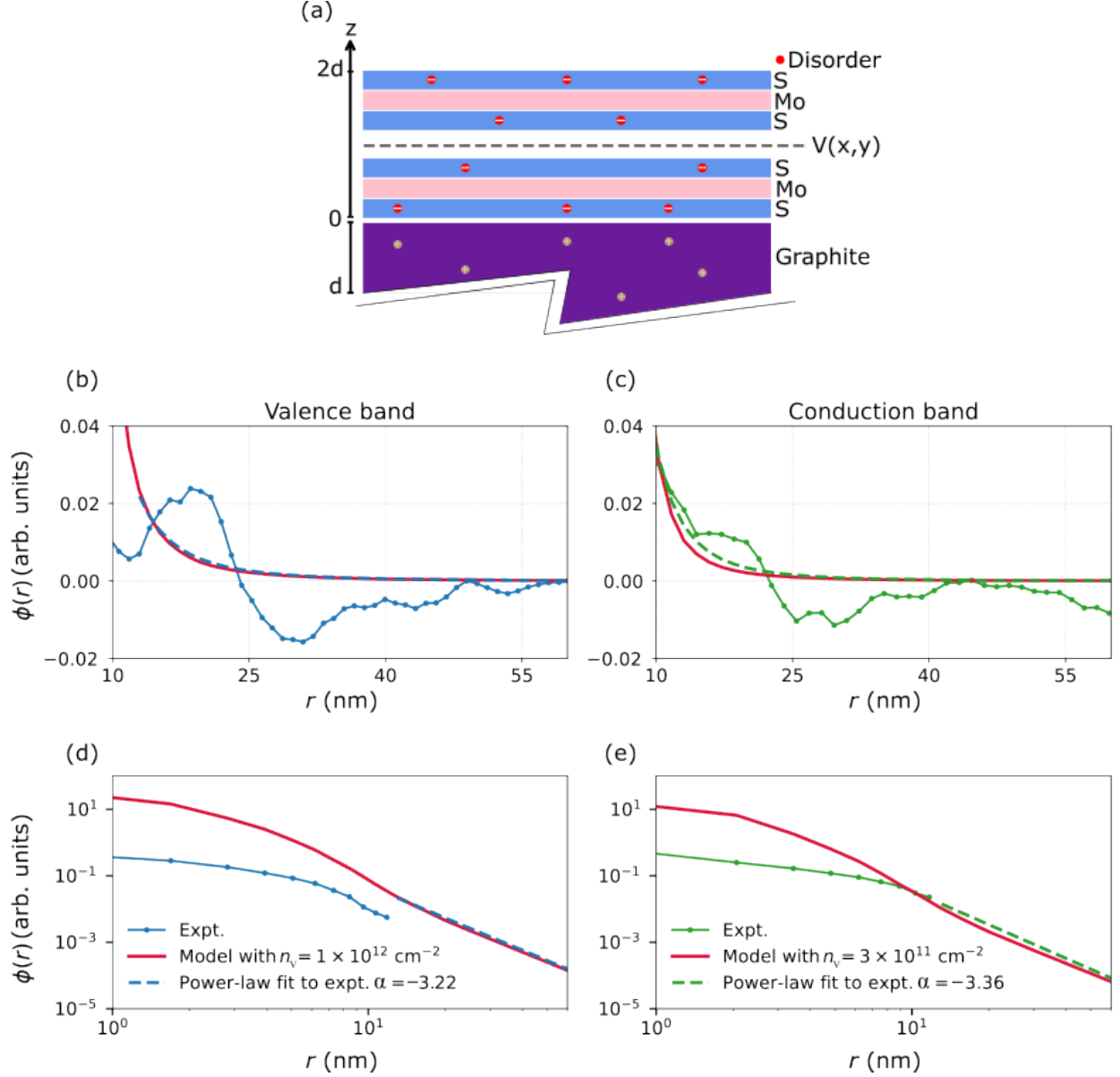


Figure 3: (a) Schematic of the electrostatic model used to estimate the electrostatic potential due to randomly-distributed charges in the sample; d is the thickness of a MoS₂ monolayer and $V(x, y)$ is the total electrostatic potential. Red dots represent randomly distributed V_S while brown dots inside the section of the graphite layer are the primary image charges. (b-e) Radially averaged disorder potential $\phi(r)$. Blue and green solid points represent the experimentally measured disorder potential $\phi(r)$, and dashed lines are power-law fits to the experimental data for $r > 10$ nm, for valence band (b,d) and conduction band (c,e) onset maps, respectively. Power-law exponents are given in the legends of d, e. Red lines in b-e are the electrostatic models that best fit the experimental profiles. In d and e we present the results for $r > 0$ nm in log-log scale with the obtained surface charge defect density, n_V in the legends.

Discussion

The results demonstrate that an out-of-plane electric potential consistent with the observed charge disorder can explain the unexpected LDOS onset shift between XM and MX domains of the same order of magnitude as that observed experimentally.

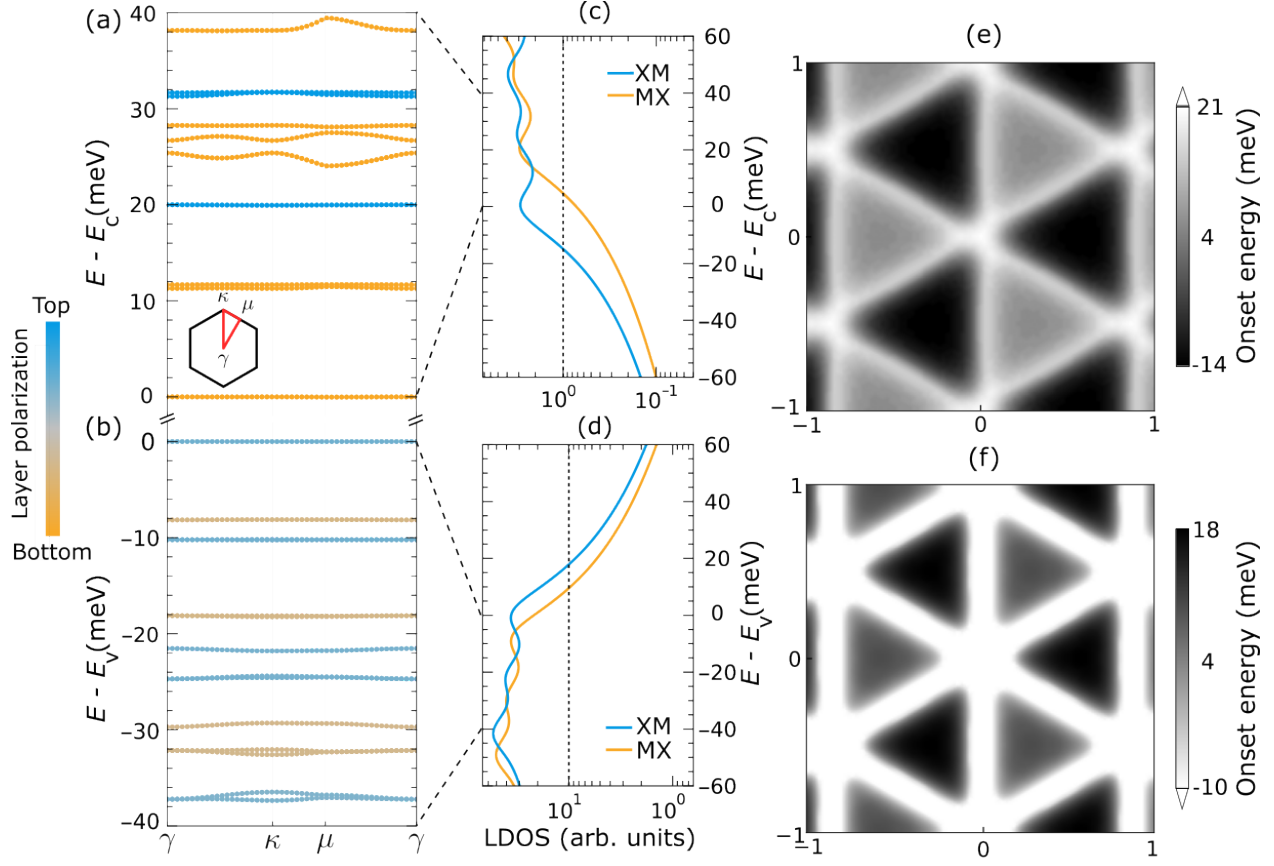


Figure 4: (a,b) Moiré conduction (a) and valence (b) minibands for tb-MoS₂ with $\theta = 0.95^\circ$ and a finite interlayer electric potential difference $V_z = 20$ meV along the mBZ path shown in the inset. The color indicates the layer polarization. (c,d) LDOS of conduction (c) and valence (d) bands, obtained assuming a Lorentzian broadening $\gamma = 10$ meV to account for charged disorder and thermal effects. The horizontal axis is in logarithmic scale. (e,f) Real-space maps (coordinates in units of the moiré length) of the onset energies at which the LDOS first crosses the dashed lines in (c,d) in the conduction (e) and valence (f) bands. Similar to Figures 1e, f, for some locations along the AA and DW regions, the color bars are not bounded in one direction (indicated by the arrow).

While the shift in LDOS onset with electric field is similar for valence and conduction bands, the mechanisms are somewhat different. For the lower conduction bands (K_c), the corresponding Wannier states are already layer-polarized even in the absence of an external field, as explained above. When an electric potential difference exists between the layers, the bands shift vertically in energy according to their dipole orientation; XM (MX) states accumulate charge on the top (bottom) layer. See SI Figure S10b. The energy difference between the oppositely polarized conduction bands corresponds to the onset shift observed in the LDOS.

For the highest valence bands (Γ_v), the bands are equally distributed in both top and bottom layers (unpolarized) at zero interlayer bias (Figure 1d), and form a graphene-like bonding and anti-bonding manifold with layer pseudospin in the x,y plane. In an electric field, the bands acquire a layer polarization, developing a subband splitting whose magnitude is proportional to the electric-potential strength. This causes the MX states to accumulate electric charge on the top layer of the stacking, while the XM states do so on the bottom layer. See SI Figure S10a. The polarization and shift in LDOS onset is reversed with respect to the conduction band, as observed experimentally (Figures 2d and e).

The calculated LDOS curves (Figures 4b, c) show no low-dispersion / flat band-related features, consistent with the averaged measurements (Figures 2d, e). This can be attributed to the intrinsic disorder observed

in our experiments.

It is probable that other sources of electric field may also significantly perturb the electronic structure of tTMDs. Particularly in STM experiments the nearby metal tip, with different work function than the sample, may produce a built-in electric field which varies with bias voltage and which may locally greatly exceed the average electric fields considered in this work. This tip electric field is highly localized, potentially to a region smaller than one moiré unit cell, and further work is needed to understand the effect of such a highly localized field on the moiré bandstructure.

Conclusions

In conclusion, our results indicate that even modest charge disorder in monolayer MoS₂ (density $\sim 10^{11}$ cm⁻², likely present in most exfoliated TMDs) can radically alter the character of the moiré bands in tTMDs at tens-of-meV energy scale. For example, the topmost moiré valence bands are transformed from a graphene-like manifold to two widely separated (much greater than bandwidth) completely layer-polarized bands. This poses profound implications for realizing certain flat band topologies in tTMDs, and indicates that care must be taken in interpreting experimental results.

Methods

Experimental methods

Sample fabrication

STM measurements are performed on a tb-MoS₂ transferred onto a ~ 30 nm thick graphite flake for electrical contact. Sample was built using Si wafers coated with 285 nm SiO₂. MoS₂ monolayers were obtained by mechanical exfoliation from high quality bulk crystals and subsequently stacked via a thin film of polycarbonate on a 6% chloroform solution using the tear-and-stack technique adapted from Ref. [57], aiming for a perfectly parallel stacking in order to obtain a near-zero twist angle. See SI Figure S1 for further sample details. The sample was then annealed in ultra high vacuum (UHV) conditions at 200°C for 2 hours and transferred to the STM chamber.

STM measurements

STM measurements were performed using an electrochemically etched tungsten tip that was calibrated on clean Au(111) to the Shockley surface state.

Coarse positioning of the STM tip over the moiré region of interest was accomplished using a capacitance-based technique adapted from Ref. [58].

STS grid measurements parameters for valence (conduction) bands are: $I_{\text{set}} = 250$ pA, 45×45 nm² (55×55 nm²) with 40×40 pixels, 3.8 mV (5.1 mV) bias step-size, 40 ms integration time, 20 mV lock-in amplitude and frequency of 793 Hz.

All the measurements here reported were performed in UHV conditions at a temperature of 4.7 K.

Onset bias calculation

The onset maps in Figures 2b and c were calculated by finding the intersection between linear fittings for the band edges of $\log(dI/dV)$ curves and arbitrary noise-floor lines at 2.5×10^{-2} (arb.units). See SI Figure S2. Top region of these maps appears brighter as the intersection with that specific noise floor is not bounded for the energy scale at which the color contrast is more visible.

The onset values presented in Figures 2d and e were found using the same method described above with arbitrary noise-floor lines at 5.25×10^{-2} (arb.units) for the valence band (d) and at 1×10^{-2} (arb.units) for the conduction band (e). The uncertainty of the average onset bias was computed assuming statistically independent measurements as $\sigma_{\text{mean}}^2 = (\sum_i n_i)^{-2} \sum_i n_i \sigma_i^2$, where n_i and σ_i^2 denote the number of points and the variance associated with region i , respectively.

Disorder density modeling

The autocorrelation function of onset maps was obtained using *numpy* library in Python 3.12.

The tb-MoS₂ is treated as two dielectric slabs, each of thickness $d \sim 6 \text{ \AA}$ [59] and monolayer MoS₂ out-of-plane relative electrical permittivity $\epsilon_r = 5.5$ [60] was used to calculate the electric potential across the stack. The contribution of the dielectric slabs to the electric potential arises from an infinite ladder of image charges with alternating sign and decreasing magnitudes. The resulting image-charge amplitudes generates a rapidly converging geometric series that we truncate at $N = 50$ terms.

The presence of a graphite substrate in electrical contact with the MoS₂ bottom layer breaks the vertical inversion symmetry of the ideal free-standing model [61]. However, this is not considered in our model as the above-mentioned graphite Thomas-Fermi screening is orders of magnitude smaller than the moiré lattice constant in our sample.

Theoretical Calculations

First-principles calculations

First-principles density functional theory (DFT) calculations were performed to simulate bilayer MoS₂, in the rhombohedral (aligned) stacking, using the ABINIT [62, 63] code, using the projector augmented wave (PAW) method [64]. ABINIT employs a plane-wave basis set, which was determined using a kinetic energy cutoff of 1000 eV. A Monkhorst-Pack k -point grid [65] of $12 \times 12 \times 1$ was used to sample the Brillouin zone. The PBE exchange-correlation functional was used [66], and the vdw-DFT-D3(BJ) [67] correction was used to treat the vdW interactions between the layers.

To sample the different possible local environments, we used 37 stacking configurations that are not related by symmetry on a triangular grid (see Figure S4), which is compatible with the C_{6v} symmetry of the adhesion potential. For each relative stacking, a geometry relaxation was performed to obtain the equilibrium layer separation, while keeping the in-plane atomic positions fixed, using a force tolerance of 1 meV/Å. Band structure calculations were then performed for each stacking, using the relaxed geometries.

Continuum model of tMoS₂

Here we briefly describe the continuum model used to calculate the band structure of tMoS₂. A detailed derivation is provided in SI.

We construct an effective Hamiltonian for aligned bilayer 2H MoS₂ near Γ_v (top of the valence band) and K_c/K'_c (bottom of the conduction band) as a function of the layer stacking ϕ . In a layer basis, this Hamiltonian can be approximated as

$$H_Q(\mathbf{k}, \phi) = \begin{bmatrix} \frac{\hbar^2 k^2}{2m_Q} + \epsilon_Q(\phi) & t_Q(-\phi) \\ t_Q(\phi) & \frac{\hbar^2 k^2}{2m_Q} + \epsilon_Q(-\phi) \end{bmatrix}, \quad (1)$$

where $\mathbf{k} = (k_x, k_y)$ is the Bloch momentum and m_Q is the effective mass at valley $Q = \Gamma_v, K_c$, $\epsilon(\phi)$ is the intralayer potential and $t(\phi)$ is the interlayer tunneling amplitude. Eq. (1) is parametrized using DFT calculations (see SI).

For small twist angles, the moiré pattern varies slowly on the interatomic scale, and we use the local stacking approximation [68]:

$$\begin{aligned} \phi(\mathbf{r}) &= R(\theta/2)\mathbf{r} - R(-\theta/2)\mathbf{r} + \mathbf{u}(\mathbf{r}) \\ &= \frac{a}{L}\hat{z} \times \mathbf{r} + \mathbf{u}(\mathbf{r}), \end{aligned} \quad (2)$$

where $R(\theta)$ is the rotation matrix for an angle θ counterclockwise about the z axis, $L = a/2 \sin(\theta/2)$ is the moiré lattice constant, and $\mathbf{u} = \mathbf{u}_1 - \mathbf{u}_2$ is the acoustic displacement field arising from lattice reconstruction.

For example, at Γ_v the continuum Hamiltonian can be written as $H_\Gamma = \sum_{s=\uparrow,\downarrow} \int d^2\mathbf{r} \psi_s^\dagger(\mathbf{r}) \mathcal{H}_\Gamma \psi_s(\mathbf{r})$ with

$$\mathcal{H}_\Gamma = -\frac{\hbar^2 \nabla^2}{2m_\Gamma} \sigma_0 + \begin{bmatrix} \epsilon(\mathbf{r}) + \frac{V_z}{2} & t(\mathbf{r}) \\ t(\mathbf{r}) & \epsilon(-\mathbf{r}) - \frac{V_z}{2} \end{bmatrix}, \quad (3)$$

where $\psi_s = (\psi_{s1}, \psi_{s2})^\top$ are fermion field operators in layer space that obey the usual anticommutation relations. We also include an interlayer bias V_z which corresponds to an electric displacement.

The moiré bands are obtained by writing down a Bloch *ansatz* for the moiré continuum theory in terms of a plane-wave expansion.

Local density of states

To compare our theory to the STM measurements described in the main text, we compute the local density of states (LDOS)

$$\rho(\mathbf{r}, E) = \sum_{n, \mathbf{k}} \delta(E - E_{n\mathbf{k}}) |\psi_{n, \mathbf{k}}(\mathbf{r})|^2, \quad (4)$$

where n is a band index (including spin, as well as valley for K_c/K'_c). Here the total wave function squared includes a sum over both layers and reciprocal moiré vectors of the plane-wave expansion. To account for disorder, we introduce a phenomenological broadening parameter γ and replace the delta function with a Lorentzian:

$$\delta(E - E_{n\mathbf{k}}) \rightarrow \frac{1}{\pi} \frac{\gamma}{(E - E_{n\mathbf{k}})^2 + \gamma^2}, \quad (5)$$

with a full width at half maximum given by 2γ .

Lattice Reconstruction

In moiré materials, reconstruction is driven by a competition between intralayer elastic energy, which prefers the rigid configuration, and interlayer stacking energy, which favors expanding regions of favorable stacking configurations. We model this atomic reconstruction of the moiré pattern with continuum elasticity [35, 37, 39, 40], which is a good approximation when the moiré period $L \gg a$ and the local stacking varies slowly compared to the interatomic scale. The continuum model, described in detail in SI, is described by the free energy

$$\mathcal{F} = \mathcal{F}_{\text{elas}}[\mathbf{u}_1] + \mathcal{F}_{\text{elas}}[\mathbf{u}_2] + \mathcal{F}_{\text{stack}}[\phi] \quad (6)$$

where $\mathcal{F}_{\text{elas}}$ is the elastic energy, $\mathbf{u}_{1,2}(\mathbf{r})$ are the displacements of layers 1 and 2, $\mathcal{F}_{\text{stack}}$ is the stacking/adhesion energy, and $\phi(\mathbf{r}) = \theta\hat{z} \times \mathbf{r} + \mathbf{u}_1(\mathbf{r}) - \mathbf{u}_2(\mathbf{r})$ is the relative stacking between the layers, in the local stacking approximation. Here, Eq. (6) was parametrized using first-principles calculations as described in SI. The effects of lattice relaxation on the band structure are accounted for in the continuum model.

Supporting information

The Supporting Information is available free of charge at: Supporting_Information.pdf. It includes:

1. Details on the experimental sample and determination of the onset bias, including photographs, and
2. theory calculations, including structural relaxation and the relaxed electronic continuum model used to calculate the local density of states as a function of interlayer bias for both the Γ_v and K_c/K'_c moiré bands.

Acknowledgment

PRV, THYV, KX, SA, MTE and MSF acknowledge support from ARC Discovery Project DP200101345. DM, SA, MTE and MSF acknowledge funding support from the ARC Centre for Future Low Energy Electronics Technologies (FLEET) CE170100039. This work was performed in part at the Melbourne Centre for Nanofabrication (MCN) in the Victorian Node of the Australian National Fabrication Facility (ANFF). D.B. acknowledges support from the NTU Startup Grant (Award Number 025661-00003). H.G-H. acknowledges financial support from the Spanish State Research Agency under grant Ramón y Cajal fellowship RYC2021-031050-I

References

- (1) Foutty, B. A.; Kometter, C. R.; Devakul, T.; Reddy, A. P.; Watanabe, K.; Taniguchi, T.; Fu, L.; Feldman, B. E. Mapping twist-tuned multiband topology in bilayer WSe₂. *Science* **2024**, *384*, 343–347, DOI: [10.1126/science.adi4728](https://doi.org/10.1126/science.adi4728).
- (2) Zhang, C.; Zhu, T.; Soejima, T.; Kahn, S.; Watanabe, K.; Taniguchi, T.; Zettl, A.; Wang, F.; Zale-tel, M. P.; Crommie, M. F. Local spectroscopy of a gate-switchable moiré quantum anomalous Hall insulator. *Nat. Commun.* **2023**, *14*, 3595, DOI: [10.1038/s41467-023-39110-3](https://doi.org/10.1038/s41467-023-39110-3).
- (3) Li, H.; Li, S.; Regan, E. C.; Wang, D.; Zhao, W.; Kahn, S.; Yumigeta, K.; Blei, M.; Taniguchi, T.; Watanabe, K., et al. Imaging two-dimensional generalized Wigner crystals. *Nature* **2021**, *597*, 650–654, DOI: [10.1038/s41586-021-03874-9](https://doi.org/10.1038/s41586-021-03874-9).
- (4) Zhao, W.; Kang, K.; Zhang, Y.; Knüppel, P.; Tao, Z.; Li, L.; Tschirhart, C. L.; Redekop, E.; Watanabe, K.; Taniguchi, T., et al. Realization of the Haldane Chern insulator in a moiré lattice. *Nat. Phys.* **2024**, *20*, 275–280, DOI: [10.1038/s41567-023-02284-0](https://doi.org/10.1038/s41567-023-02284-0).
- (5) Guo, X.; Ge, H.; Watanabe, K.; Taniguchi, T.; Chen, Z.; Gu, J. Mott insulator polariton in a MoSe₂/WS₂ moiré Lattice. *Nano Lett.* **2025**, *25*, 15680–15685, DOI: [10.1021/acs.nanolett.5c04233](https://doi.org/10.1021/acs.nanolett.5c04233).
- (6) Guo, Y.; Pack, J.; Swann, J.; Holtzman, L.; Cothrine, M.; Watanabe, K.; Taniguchi, T.; Mandrus, D. G.; Barmak, K.; Hone, J., et al. Superconductivity in 5.0° twisted bilayer WSe₂. *Nature* **2025**, *637*, 839–845, DOI: [10.1038/s41586-024-08116-2](https://doi.org/10.1038/s41586-024-08116-2).
- (7) Thompson, E.; Chu, K. T.; Mesple, F.; Zhang, X.-W.; Hu, C.; Zhao, Y.; Park, H.; Cai, J.; Anderson, E.; Watanabe, K., et al. Microscopic signatures of topology in twisted MoTe₂. *Nat. Phys.* **2025**, *21*, 1224–1230, DOI: [10.1038/s41567-025-02877-x](https://doi.org/10.1038/s41567-025-02877-x).
- (8) Cao, Y.; Fatemi, V.; Fang, S.; Watanabe, K.; Taniguchi, T.; Kaxiras, E.; Jarillo-Herrero, P. Unconventional superconductivity in magic-angle graphene superlattices. *Nature* **2018**, *556*, 43–50, DOI: [10.1038/nature26160](https://doi.org/10.1038/nature26160).
- (9) Cao, Y.; Fatemi, V.; Demir, A.; Fang, S.; Tomarken, S. L.; Luo, J. Y.; Sanchez-Yamagishi, J. D.; Watanabe, K.; Taniguchi, T.; Kaxiras, E., et al. Correlated insulator behaviour at half-filling in magic-angle graphene superlattices. *Nature* **2018**, *556*, 80–84, DOI: doi.org/10.1038/nature26154.
- (10) Xian, L.; Claassen, M.; Kiese, D.; Scherer, M. M.; Trebst, S.; Kennes, D. M.; Rubio, A. Realization of nearly dispersionless bands with strong orbital anisotropy from destructive interference in twisted bilayer MoS₂. *Nat. Commun.* **2021**, *12*, 5644, DOI: [10.1038/s41467-021-25922-8](https://doi.org/10.1038/s41467-021-25922-8).
- (11) Zhang, Y.; Zhan, Z.; Guinea, F.; Silva-Guillén, J. Á.; Yuan, S. Tuning band gaps in twisted bilayer MoS₂. *Phys. Rev. B* **2020**, *102*, 235418, DOI: [10.1103/PhysRevB.102.235418](https://doi.org/10.1103/PhysRevB.102.235418).
- (12) Andrei, E. Y.; Efetov, D. K.; Jarillo-Herrero, P.; MacDonald, A. H.; Mak, K. F.; Senthil, T.; Tutuc, E.; Yazdani, A.; Young, A. F. The marvels of moiré materials. *Nat. Rev. Mater.* **2021**, *6*, 201–206, DOI: [10.1038/s41578-021-00284-1](https://doi.org/10.1038/s41578-021-00284-1).
- (13) Shah, S. J.; Chen, J.; Xie, X.; Oyang, X.; Ouyang, F.; Liu, Z.; Wang, J.-T.; He, J.; Liu, Y. Progress and prospects of moiré superlattices in twisted TMD heterostructures. *Nano Res.* **2024**, *17*, 10134–10161, DOI: [10.1007/s12274-024-6936-3](https://doi.org/10.1007/s12274-024-6936-3).
- (14) Liu, S.; Liu, Y.; Holtzman, L.; Li, B.; Holbrook, M.; Pack, J.; Taniguchi, T.; Watanabe, K.; Dean, C. R.; Pasupathy, A. N., et al. Two-step flux synthesis of ultrapure transition-metal dichalcogenides. *ACS nano* **2023**, *17*, 16587–16596, DOI: [10.1021/acsnano.3c02511](https://doi.org/10.1021/acsnano.3c02511).
- (15) Holbrook, M.; Holtzman, L. N.; Hou, B.; Nashabeh, L.; Qiu, D. Y.; Barmak, K.; Pasupathy, A. N.; Hone, J. C. Revealing Substitutional oxygen as the dominant defect in flux-grown transition metal diselenides. *Nano Lett.* **2025**, *25*, 13795–13801, DOI: [10.1021/acs.nanolett.5c03126](https://doi.org/10.1021/acs.nanolett.5c03126).
- (16) Xu, K.; Holbrook, M.; Holtzman, L. N.; Pasupathy, A. N.; Barmak, K.; Hone, J. C.; Rosenberger, M. R. Validating the use of conductive atomic force microscopy for defect quantification in 2D materials. *ACS Nano* **2023**, *17*, 24743–24752, DOI: [10.1021/acsnano.3c05056](https://doi.org/10.1021/acsnano.3c05056).

(17) Wang, V.; Lin, J.; Liang, E.; Ohno, T.; Nara, J.; Geng, W. Effect of direct interlayer coupling on the moiré potentials in twisted WSe₂/MoSe₂ heterobilayers. *Physica B: Condensed Matter* **2025**, *699*, 416873, DOI: 10.1016/j.physb.2024.416873.

(18) De la Torre, A.; Kennes, D. M.; Malic, E.; Kar, S. Advanced Characterization of the Spatial Variation of Moiré Heterostructures and Moiré Excitons. *Small* **2025**, *21*, 2570216, DOI: 10.1002/smll.202401474.

(19) Zhang, Y.; Brar, V. W.; Girit, C.; Zettl, A.; Crommie, M. F. Origin of spatial charge inhomogeneity in graphene. *Nat. Phys.* **2009**, *5*, 722–726, DOI: 10.1038/nphys1365.

(20) Edmonds, M. T.; Collins, J. L.; Hellerstedt, J.; Yudhistira, I.; Gomes, L. C.; Rodrigues, J. N.; Adam, S.; Fuhrer, M. S. Spatial charge inhomogeneity and defect states in topological Dirac semimetal thin films of Na₂Bi. *Sci. Adv.* **2017**, *3*, eaao6661, DOI: 10.1126/sciadv.aa06661.

(21) Holbrook, M.; Ingham, J.; Kaplan, D.; Holtzman, L.; Bierman, B.; Olson, N.; Nashabeh, L.; Liu, S.; Zhu, X.; Rhodes, D., et al. Real-space imaging of the band topology of transition metal dichalcogenides, 2024, DOI: 10.48550/arXiv.2412.02813.

(22) Xiang, Z.; Li, H.; Xiao, J.; Naik, M. H.; Ge, Z.; He, Z.; Chen, S.; Nie, J.; Li, S.; Jiang, Y., et al. Imaging quantum melting in a disordered 2D Wigner solid. *Science* **2025**, *388*, 736–740, DOI: 10.1126/science.ado7136.

(23) Zograf, G.; Yankovich, A. B.; Küçüköz, B.; Agrawal, A. V.; Polyakov, A. Y.; Ciers, J.; Eriksson, F.; Haglund, Å.; Erhart, P.; Antosiewicz, T. J., et al. Defect-assisted reversible phase transition in mono- and few-layer ReS₂. *npj 2D Materials and Applications* **2025**, *9*, 3, DOI: 10.1038/s41699-025-00524-w.

(24) Vancsó, P.; Magda, G. Z.; Pető, J.; Noh, J.-Y.; Kim, Y.-S.; Hwang, C.; Biró, L. P.; Tapasztó, L. The intrinsic defect structure of exfoliated MoS₂ single layers revealed by scanning tunneling microscopy. *Sci. Rep.* **2016**, *6*, 29726, DOI: 10.1038/srep29726.

(25) Pei, D.; Wang, B.; Zhou, Z.; He, Z.; An, L.; He, S.; Chen, C.; Li, Y.; Wei, L.; Liang, A., et al. Observation of Γ -valley moiré bands and emergent hexagonal lattice in twisted transition metal dichalcogenides. *Phys. Rev. X* **2022**, *12*, 021065, DOI: 10.1103/PhysRevX.12.021065.

(26) Feraco, G.; De Luca, O.; Przybysz, P.; Jafari, H.; Zheliuk, O.; Wang, Y.; Schädlich, P.; Dudin, P.; Avila, J.; Ye, J., et al. Nano-ARPES investigation of structural relaxation in small angle twisted bilayer tungsten disulfide. *Phys. Rev. Mater.* **2024**, *8*, 124004, DOI: 10.1103/PhysRevMaterials.8.124004.

(27) Li, T.; Jiang, S.; Li, L.; Zhang, Y.; Kang, K.; Zhu, J.; Watanabe, K.; Taniguchi, T.; Chowdhury, D.; Fu, L., et al. Continuous Mott transition in semiconductor moiré superlattices. *Nature* **2021**, *597*, 350–354, DOI: 10.1038/s41586-021-03853-0.

(28) Tang, Y.; Li, L.; Li, T.; Xu, Y.; Liu, S.; Barmak, K.; Watanabe, K.; Taniguchi, T.; MacDonald, A. H.; Shan, J., et al. Simulation of Hubbard model physics in WSe₂/WS₂ moiré superlattices. *Nature* **2020**, *579*, 353–358, DOI: 10.1038/s41586-020-2085-3.

(29) Li, E.; Hu, J.-X.; Feng, X.; Zhou, Z.; An, L.; Law, K. T.; Wang, N.; Lin, N. Lattice reconstruction induced multiple ultra-flat bands in twisted bilayer WSe₂. *Nat. Commun.* **2021**, *12*, 5601, DOI: 10.1038/s41467-021-25924-6.

(30) Tilak, N.; Li, G.; Taniguchi, T.; Watanabe, K.; Andrei, E. Y. Moiré potential, lattice relaxation, and layer polarization in marginally twisted MoS₂ bilayers. *Nano Lett.* **2022**, *23*, 73–81, DOI: 10.1021/acs.nanolett.2c03676.

(31) Liu, X.; Liu, S.; Xiao, Y.; Xu, C.; Wu, J.; Li, K.; Li, S.-Y.; Pan, A. Probing the special angle in twisted bilayer MoS₂ via angle-dependent scanning tunneling microscopy studies. *Sci. China Phys. Mech. Astron.* **2025**, *68*, 226811, DOI: 10.1007/s11433-024-2529-9.

(32) Lu, C.-P.; Li, G.; Mao, J.; Wang, L.-M.; Andrei, E. Y. Bandgap, mid-gap states, and gating effects in MoS₂. *Nano Lett.* **2014**, *14*, 4628–4633, DOI: 10.1021/nl501659n.

(33) McDonnell, S.; Addou, R.; Buie, C.; Wallace, R. M.; Hinkle, C. L. Defect-dominated doping and contact resistance in MoS₂. *ACS nano* **2014**, *8*, 2880–2888, DOI: 10.1021/nn500044q.

(34) Addou, R.; Colombo, L.; Wallace, R. M. Surface defects on natural MoS₂. *ACS applied materials & interfaces* **2015**, *7*, 11921–11929, DOI: 10.1021/acsami.5b01778.

(35) Carr, S.; Massatt, D.; Torrisi, S. B.; Cazeaux, P.; Luskin, M.; Kaxiras, E. Relaxation and domain formation in incommensurate two-dimensional heterostructures. *Phys. Rev. B* **2018**, *98*, 224102, DOI: 10.1103/PhysRevB.98.224102.

(36) Cazeaux, P.; Clark, D.; Engelke, R.; Kim, P.; Luskin, M. Relaxation and domain wall structure of bilayer moiré systems. *J. Elast.* **2023**, *154*, 443–466, DOI: 10.1007/s10659-023-10013-0.

(37) De Beule, C.; Pallewela, G. N.; Al Ezzi, M. M.; Peng, L.; Mele, E. J.; Adam, S. Theory for lattice relaxation in marginal twist moirés, 2025, DOI: 10.48550/arXiv.2503.19162.

(38) Le, O. K.; Chihiaia, V.; Pham-Ho, M.-P.; Son, D. N. Electronic and optical properties of monolayer MoS₂ under the influence of polyethyleneimine adsorption and pressure. *RSC Adv.* **2020**, *10*, 4201–4210, DOI: 10.1039/C9RA09042H.

(39) Nam, N. N. T.; Koshino, M. Lattice relaxation and energy band modulation in twisted bilayer graphene. *Phys. Rev. B* **2017**, *96*, 075311, DOI: 10.1103/PhysRevB.96.075311.

(40) Bennett, D. Theory of polar domains in moiré heterostructures. *Phys. Rev. B* **2022**, *105*, 235445, DOI: 10.1103/PhysRevB.105.235445.

(41) Zhu, H.; Zhou, C.; Huang, X.; Wang, X.; Xu, H.; Lin, Y.; Yang, W.; Wu, Y.; Lin, W.; Guo, F. Evolution of band structures in MoS₂-based homo- and heterobilayers. *J. Phys. D: Appl. Phys.* **2016**, *49*, 065304, DOI: 10.1088/0022-3727/49/6/065304.

(42) Venkateswarlu, S.; Honecker, A.; Trambly-de Laissardière, G. Electronic localization in twisted bilayer MoS₂ with small rotation angle. *Phys. Rev. B* **2020**, *102*, 081103, DOI: 10.1103/PhysRevB.102.081103.

(43) Naik, M. H.; Jain, M. Ultraflatbands and shear solitons in moiré patterns of twisted bilayer transition metal dichalcogenides. *Phys. Rev. Lett.* **2018**, *121*, 266401, DOI: 10.1103/PhysRevLett.121.266401.

(44) Zhang, Y.; Liu, T.; Fu, L. Electronic structures, charge transfer, and charge order in twisted transition metal dichalcogenide bilayers. *Phys. Rev. B* **2021**, *103*, 155142, DOI: 10.1103/PhysRevB.103.155142.

(45) Tang, S.; Zhang, C.; Wong, D.; Pedramrazi, Z.; Tsai, H.-Z.; Jia, C.; Moritz, B.; Claassen, M.; Ryu, H.; Kahn, S., et al. Quantum spin Hall state in monolayer 1T'-WTe₂. *Nat. Phys.* **2017**, *13*, 683–687, DOI: 10.1038/nphys4174.

(46) Ugeda, M. M.; Bradley, A. J.; Zhang, Y.; Onishi, S.; Chen, Y.; Ruan, W.; Ojeda-Aristizabal, C.; Ryu, H.; Edmonds, M. T.; Tsai, H.-Z., et al. Characterization of collective ground states in single-layer NbSe₂. *Nat. Phys.* **2016**, *12*, 92–97, DOI: 10.1038/nphys3527.

(47) Thomas, J. C.; Chen, W.; Xiong, Y.; Barker, B. A.; Zhou, J.; Chen, W.; Rossi, A.; Kelly, N.; Yu, Z.; Zhou, D., et al. A substitutional quantum defect in WS₂ discovered by high-throughput computational screening and fabricated by site-selective STM manipulation. *Nat. Commun.* **2024**, *15*, 3556, DOI: 10.1038/s41467-024-47876-3.

(48) Zhou, W.; Zou, X.; Najmaei, S.; Liu, Z.; Shi, Y.; Kong, J.; Lou, J.; Ajayan, P. M.; Yakobson, B. I.; Idrobo, J.-C. Intrinsic structural defects in monolayer molybdenum disulfide. *Nano Lett.* **2013**, *13*, 2615–2622, DOI: 10.1021/nl4007479.

(49) Komsa, H.-P.; Krasheninnikov, A. V. Native defects in bulk and monolayer MoS₂ from first principles. *Phys. Rev. B* **2015**, *91*, 125304, DOI: 10.1103/PhysRevB.91.125304.

(50) Carozo, V.; Wang, Y.; Fujisawa, K.; Carvalho, B. R.; McCreary, A.; Feng, S.; Lin, Z.; Zhou, C.; Perea-López, N.; Elías, A. L., et al. Optical identification of sulfur vacancies: Bound excitons at the edges of monolayer tungsten disulfide. *Sci. Adv.* **2017**, *3*, e1602813, DOI: 10.1126/sciadv.1602813.

(51) Kim, M.; Xu, S. G.; Berdyugin, A. I.; Principi, A.; Slizovskiy, S.; Xin, N.; Kumaravadivel, P.; Kuang, W.; Hamer, M.; Krishna Kumar, R., et al. Control of electron-electron interaction in graphene by proximity screening. *Nat. Commun.* **2020**, *11*, 2339, DOI: 10.1038/s41467-020-16083-5.

(52) Gao, Q.; Zhang, Z.; Xu, X.; Song, J.; Li, X.; Wu, Y. Scalable high performance radio frequency electronics based on large domain bilayer MoS₂. *Nat. Commun.* **2018**, *9*, 4778, DOI: 10.1038/s41467-018-07290-6.

(53) Jackson, J. D.; Fox, R. F., *Classical Electrodynamics*, 3rd; John Wiley & Sons: New York, 1999; Chapter 2, pp 57–62.

(54) Aryeetey, F.; Ignatova, T.; Aravamudhan, S. Quantification of defects engineered in single layer MoS₂. *RSC Adv.* **2020**, *10*, 22996–23001, DOI: 10.1039/DORA03372C.

(55) Picker, J.; Gan, Z.; Neumann, C.; George, A.; Turchanin, A. Low defect density in MoS₂ monolayers grown on Au(111) by metal-organic chemical vapor deposition. *Micron* **2024**, *186*, 103708, DOI: 10.1016/j.micron.2023.103708.

(56) Zhang, X.; Xu, J.; Zhi, A.; Wang, J.; Wang, Y.; Zhu, W.; Han, X.; Tian, X.; Bai, X.; Sun, B., et al. Low-defect-density monolayer MoS₂ wafer by oxygen-assisted growth-repair strategy. *Adv. Sci.* **2024**, *11*, 2408640, DOI: 10.1002/advs.202408640.

(57) Cao, Y.; Luo, J.; Fatemi, V.; Fang, S.; Sanchez-Yamagishi, J.; Watanabe, K.; Taniguchi, T.; Kaxiras, E.; Jarillo-Herrero, P. Superlattice-induced insulating states and valley-protected orbits in twisted bilayer graphene. *Phys. Rev. Lett.* **2016**, *117*, 116804, DOI: 10.1103/PhysRevLett.117.116804.

(58) Li, G.; Luican, A.; Andrei, E. Y. Self-navigation of a scanning tunneling microscope tip toward a micron-sized graphene sample. *Rev. Sci. Instrum.* **2011**, *82*, 073701, DOI: 10.1063/1.3605664.

(59) Al-Dulaimi, N.; Lewis, D. J.; Zhong, X. L.; Malik, M. A.; O'Brien, P. Chemical vapour deposition of rhenium disulfide and rhenium-doped molybdenum disulfide thin films using single-source precursors. *J. Mater. Chem. C* **2016**, *4*, 2312–2318, DOI: 10.1039/C6TC00489J.

(60) Laturia, A.; Vandenberghe, W. G. *2017 International Conference on Simulation of Semiconductor Processes and Devices (SISPAD)*, 2017, pp 337–340, DOI: 10.23919/SISPAD.2017.8085333.

(61) Zhang, C.; Johnson, A.; Hsu, C.-L.; Li, L.-J.; Shih, C.-K. Direct imaging of band profile in single layer MoS₂ on graphite: quasiparticle energy gap, metallic edge states, and edge band bending. *Nano Lett.* **2014**, *14*, 2443–2447, DOI: 10.1021/nl501133c.

(62) Gonze, X.; et al. The Abinitproject: Impact, environment and recent developments. *Comput. Phys. Commun.* **2020**, *248*, 107042, DOI: 10.1016/j.cpc.2019.107042.

(63) Verstraete, M. J.; Abreu, J.; Allemand, G. E.; Amadon, B.; Antonius, G.; Azizi, M.; Baguet, L.; Barat, C.; Bastogne, L.; Béjaud, R., et al. Abinit 2025: New capabilities for the predictive modeling of solids and nanomaterials. *J. Chem. Phys.* **2025**, *163*, DOI: 10.1063/5.0288278.

(64) Torrent, M.; Jollet, F.; Bottin, F.; Zérah, G.; Gonze, X. Implementation of the projector augmented-wave method in the ABINIT code: Application to the study of iron under pressure. *Comput. Mater. Sci.* **2008**, *42*, 337–351, DOI: 10.1016/j.commatsci.2007.07.020.

(65) Monkhorst, H. J.; Pack, J. D. Special points for Brillouin-zone integrations. *Phys. Rev. B* **1976**, *13*, 5188, DOI: 10.1103/PhysRevB.13.5188.

(66) Perdew, J. P.; Burke, K.; Ernzerhof, M. Generalized gradient approximation made simple. *Phys. Rev. Lett.* **1996**, *77*, 3865–3868, DOI: 10.1103/PhysRevLett.77.3865.

(67) Becke, A. D.; Johnson, E. R. A simple effective potential for exchange. *J. Chem. Phys.* **2006**, *124*, 221101, DOI: 10.1063/1.2213970.

(68) Jung, J.; DaSilva, A. M.; MacDonald, A. H.; Adam, S. Origin of band gaps in graphene on hexagonal boron nitride. *Nat. Commun.* **2015**, *6*, 6308, DOI: 10.1038/ncomms7308.